AGU PUBLICATIONS

JGR

Journal of Geophysical Research: Oceans

RESEARCH ARTICLE

10.1002/2016JC011990

Key Points:
- Irreversible mixing in steady stratified flows over topography is investigated in three regimes
- Local mixing overwhelms remote mixing in a large range of forcing parameters
- Nonlinear mechanisms near ocean bathymetry may induce greater mixing than radiating lee waves

Correspondence to:
Y. Dossmann,
yvan.dossmann@univ-lorraine.fr

Citation:
Dossmann, Y., M. G. Rosevear, R. W. Griffiths, A. McC. Hogg, G. O. Hughes, and M. Copeland (2016), Experiments with mixing in stratified flow over a topographic ridge, *J. Geophys. Res. Oceans*, *121*, 6961–6977, doi:10.1002/2016JC011990.

Received 23 MAY 2016
Accepted 23 AUG 2016
Accepted article online 25 AUG 2016
Published online 22 SEP 2016

© 2016. American Geophysical Union. All Rights Reserved.

Experiments with mixing in stratified flow over a topographic ridge

Yvan Dossmann[1,2,3], Madelaine G. Rosevear[1], Ross W. Griffiths[1], Andrew McC. Hogg[1], Graham O. Hughes[1,4], and Michael Copeland[1]

[1]Research School of Earth Sciences, Australian National University, Canberra, Australian Capital Territory, Australia, [2]Univ Lyon, ENS de Lyon, Univ Claude Bernard, CNRS, Laboratoire de Physique, Lyon, France, [3]Now at LEMTA - Université de Lorraine CNRS - UMR 7563, Nancy, France, [4]Now at Department of Civil and Environmental Engineering, Imperial College London, South Kensington, London, UK

Abstract The interaction of quasi-steady abyssal ocean flow with submarine topography is expected to generate turbulent mixing in the ocean. This mixing may occur locally, close to topography, or via breaking quasi-steady lee waves that can carry energy into the ocean interior. There is currently no theoretical, or empirically derived, prediction for the relative amounts of local and interior mixing. We report measurements of the mixing rate in laboratory experiments with a topographic ridge towed through a density stratification. The experiments span three parameter regimes including linear lee waves, nonlinear flow and an evanescent regime in which wave radiation is weak. Full field density measurements provide the depth-dependence of energy loss to turbulent mixing, allowing separation of the local mixing in the turbulent wake and remote mixing by wave radiation. Remote mixing is significant only for a narrow band of forcing parameters where the flow speed is resonant with internal waves; in all other parameter regimes local mixing close to the topography is dominant. The results suggest that mixing by local nonlinear mechanisms close to abyssal ocean topography may be much greater than the remote mixing by quasi-steady lee waves.

1. Introduction

Irreversible mixing of the density stratification is thought to play an important role in governing the general oceanic circulation. Mixing is induced by a variety of physical processes [*Munk and Wunsch*, 1998] including internal waves generated by tidal interactions with topography which radiate energy into the ocean interior causing mixing where they break [*Polzin et al.*, 1997; *Gregg and Ozsoy*, 1999], surface wind fluctuations that generate downward propagating internal waves [*Polton et al.*, 2008], turbulent downslope flows [*Price and Baringer*, 1994], and topographically steered abyssal overflows [*Bryden and Nurser*, 2003]. More recently, it has been proposed that the interaction between geostrophic eddies and bottom topography can also generate internal lee waves, which may in turn enhance mixing [*Nikurashin and Ferrari*, 2010a,2010b]. In contrast to tidally generated internal waves (also known as internal tides) the lee waves induced by eddies require small lateral topographic scales. At these scales, bottom velocities induced by geostrophic eddies vary slowly, and thus produce a lee wave field that is quasi-steady. A fraction of the lee waves energy can then be lost to irreversible mixing in the ocean interior through the generation of turbulence in overturning events.

Estimates of the rates of water-mass transformation caused by quasi-steady lee wave-induced mixing [*Nikurashin and Ferrari*, 2011, 2013] are based on a linear theory for the energy flux into lee waves in stratified flow over two-dimensional topography [*Bell*, 1975]. This energy flux is then translated into an estimate of the turbulent diffusion coefficient using a semiempirical parameterization that was designed for internal tides [*St. Laurent et al.*, 2002]. Using this parameterization, it has been proposed that breaking of quasi-steady lee waves contributes more than one third of the global internal wave-induced mixing, the remainder being caused by internal tides [*Nikurashin and Ferrari*, 2011, 2013]. Parameterizations based on *Bell* [1975] have also been implemented in prognostic global ocean models which highlight the potential role of lee wave-driven mixing on the stratification and overturning circulation, along with a need for stronger physical foundations of parameterizations [*Melet et al.*, 2014].

There are a number of other mechanisms for mixing that are present when quasi-steady flows interact with bottom topography. These mixing processes depend upon the dynamics of flow regimes that can occur, which are governed by the Froude number based on ridge height [*Gheusi et al*., 2000; *Vosper*, 2004]. For example, the generation of internal lee waves can be accompanied by highly nonlinear rotors in the lee of a ridge [*Eiff et al*., 2005; *Knigge et al*., 2010]. At small Froude number, the most dense fluid may be blocked by the ridge, creating an upstream jet that accelerates as it passes over the ridge [*Baines and Hoinka*, 1985]. Turbulent mixing is thereby generated in the wake and a stationary mixed region downstream of the crest [*Winters and Armi*, 2013, 2014]. In addition, at sufficiently high Froude number, the topography may generate frequencies that are too high to propagate as internal lee waves, implying that this energy must be dissipated near the topography. Thus, linear lee waves occur over only a limited region of parameter space, leaving a wide range of conditions unexplored.

An alternative parameterization for quasi-steady oceanic lee waves, based on *Garner*'s [2005] scheme for topographic interaction in the atmosphere, was introduced by *Trossman et al*. [2015]. Their scheme includes nonlinear processes such as topographic blocking, which produces higher estimates of turbulent dissipation in the lower 1000 m of the ocean than schemes based on *Bell* [1975]. The *Garner* [2005] scheme has been shown to reduce kinetic energy in the modeled abyssal ocean owing to quasi-steady lee wave drag [*Trossman et al*., 2016], but the mixing induced by this process is yet to be quantified. *Trossman et al*. [2015] make the case that better observations, particularly close to topography, are needed to validate lee wave closure schemes.

The parameterization of *St. Laurent et al*. [2002] requires specification of three parameters: the fraction of energy that is dissipated locally, q, the turbulent mixing efficiency, Γ and the vertical structure ($F(z)$) of mixing in the water column. The local dissipation fraction was estimated at $q=0.3\pm0.1$ from ocean measurements of internal tides breaking in the Brazil Basin [*St. Laurent et al*., 2002], and smaller values of q may be possible in situations where conversion of energy to low mode internal tides dominates [*Nikurashin and Legg*, 2011]. *Waterman et al*. [2013] argue that q will depend on the roughness of topography and spatial variability, with observations from the Hawaiian Ocean Mixing Experiment suggesting values as small as $q \approx 0.05$ [*St. Laurent et al*., 2002]. However, there has been no attempt to empirically measure either q, or the vertical structure function $F(z)$ for the case of quasi-steady lee waves. The only available calibrations come from numerical simulations for an idealized quasi-steady flow with lee wave breaking events which estimate $q=0.3\pm0.1$ [*Nikurashin and Ferrari*, 2010a], although it may be as large as 0.5 [*Nikurashin and Ferrari*, 2011].

Oceanographers commonly rely on an assumption of an average mixing efficiency in the ocean, $\Gamma=0.2$ [e.g., *Polzin et al*., 1997]. However, there is scant evidence that Γ takes on the same value for different mixing mechanisms [*Ivey et al*., 2008] and, where Γ has been directly measured in high Reynolds number flows, considerable differences in efficiency are found. The value $\Gamma=0.2$ was obtained in experiments with zero-mean-shear turbulence [*Linden*, 1979]. Other experiments give $\Gamma=0.11\pm0.01$ (in the absence of bottom topography) and $\Gamma=0.08\pm0.01$ (in the presence of a topographic ridge) for shear instability in baroclinic exchange flows through constrictions at large Reynolds numbers [*Prastowo et al*., 2008, 2009], and $\Gamma=[0.03, 0.08]$ for breaking quasi-interfacial waves in a two-layer configuration [*Hult et al*., 2011a,2011b]. Convective processes tend to give rise to relatively large mixing efficiencies [*Lawrie and Dalziel*, 2011; *Davies Wykes and Dalziel*, 2014]. Convection, rather than shear production of turbulence, can be a major cause of the mixing in internal wave overturning [*Gayen and Sarkar*, 2010; *Chalamalla and Sarkar*, 2015]. *Bluteau et al*. [2013] reported field measurements of turbulent mixing efficiencies at an energetic hotspot. They highlighted that a variable mixing efficiency with typical values of 0.01 can lead to realistic transformations of water masses. These transformations were overestimated by an order of magnitude when using the constant mixing efficiency $\Gamma=0.2$. An appropriate value of Γ in the deep ocean will therefore depend on whether waves or mean shear flow cause most of the mixing.

In summary, accurate parameterization of mixing by quasi-steady lee waves in the ocean is compromised by a lack of systematic empirical studies that span the full range of dynamical behaviour. In this paper, we address this problem using a series of laboratory experiments to directly measure the mixing induced by a quasi-steady stratified flow over a ridge, and to understand the dependence of mixing on the flow dynamics. We aim to partition the mixing into near-topography contributions and remote mixing (radiated by quasi-steady internal lee waves). The experimental setup and measurement techniques are introduced in section 2. In section 3 the flow is described and we evaluate the irreversible changes of the background

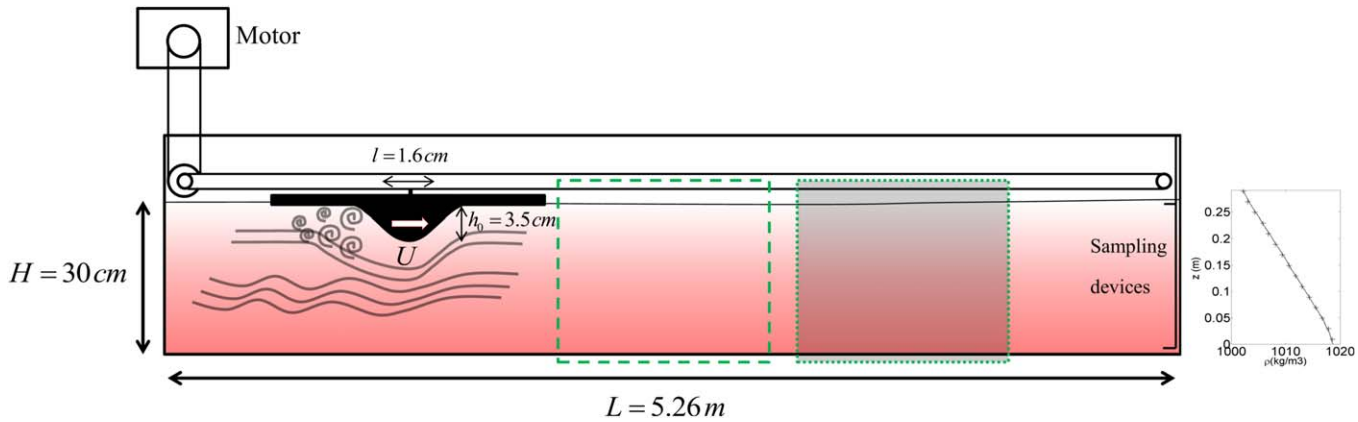

Figure 1. Experimental setup (not to scale). The tank is filled with a linear salinity gradient (inset at right). Red dye is a passive tracer of salt. (middle) The rectangle in green broken line indicates the area of density field measurements and (right) the shaded green rectangle indicates the location of shadowgraph photographs.

stratification due to mixing. In section 4 we consider the relative importance of remote mixing induced by lee waves and local mixing in the wake of the topography, as well as the previously defined local dissipation efficiency q. Conclusions are drawn in section 5.

2. Experimental Method

An idealized two-dimensional ridge is towed at a constant speed through initially stationary and uniformly stratified water in a long channel. For experimental convenience the ridge is inverted (compared to ocean floor topography) and moves along the upper surface of the water, as shown in Figure 1. The experiments are nonrotating, which means that there is no lower limit to the frequency of radiating lee waves and that potential vorticity dynamics do not lead to velocity components in the along-ridge (cross-stream) direction.

2.1. Laboratory Apparatus

The channel was 5.26 m long, 20 cm wide and 40 cm deep. The laboratory room and water temperature were controlled at 20±1°C. Two 200 L drums, one initially filled with brine and the other with freshwater, were used to create a linear stratification in the channel following the double-bucket technique [*Oster*, 1965]. A small amount of red food dye was added to the brine drum and serves as a passive tracer of the salt. The dye concentration everywhere in the channel flow was a proxy for salinity and density. Accurate measurements of the density field were made using the attenuation of transmitted light by the dissolved tracer.

The channel was filled to a depth of $H = 30$ cm. For most experiments the initially uniform Brunt-Vaisala frequency was $N_0 \equiv \sqrt{(-g/\rho_0)(d\bar{\rho}/dz)} \approx 1$ rad s^{-1}, where $g = 9.8$ m s^{-2} is the acceleration due to gravity, $\rho_0 = 1000$ kg m^{-3} the reference density, $\bar{\rho}(z)$ is the density profile and z is the vertical coordinate.

Two ridges were used, each two-dimensional with a Gaussian profile given by

$$h(x) = h_0 \exp\left(-\left(\frac{x}{l_r}\right)^2\right), \tag{1}$$

where x is the horizontal coordinate with the origin at the center of the ridge base and $h_0 = 3.5$ cm is the maximum height. Twenty seven experiments were carried out with a ridge of e-folding width $l_r = 5.0$ cm, and 10 experiments with a wider ridge having $l_r = 16$ cm. The ridge was attached at the center of a horizontal plate 80 cm long so as to allow an upstream boundary layer to develop during motion in either direction. The weight of the floating ridge and plate was adjusted so that the ridge was completely submerged and the base of the plate was 2 to 3 mm beneath the surface of the water. The ridge was attached to a taut wire connected to a "SmartMotor" via rotating cylinders that towed the ridge at a velocity controlled by a preprogrammed computer interface. The ridge-plate assembly was accelerated to, and decelerated from, the set towing speed over distances of approximately 150 mm at the start and end of each transit.

Shadowgraph visualizations gave qualitative information on the locations of turbulence in the same experiments as those used for density fields. The latter technique relies on the deflection of light rays travelling through the stratified flow and projected onto a recording plane. The illumination pattern allows for a qualitative survey of the flow dynamics [*Merzkirch*, 1981]. In a further set of experiments layers of coloured dyes introduced during the filling procedure marked density layers and provided direct visualization of the displacement of isopycnal surfaces. The advection and mixing of dyes of different colour in these runs also showed, in a qualitative sense, the location and intensity of diapycnal mixing.

2.2. Light Attenuation Technique

The light attenuation measurements gave density fields before, during and after transits of the ridge, at a high spatial resolution limited only by the digital camera sensor [*Allgayer and Hunt*, 1991]. This method has been previously applied to infer dye concentration and density fields from attenuation measurements [e.g., *Hacker et al*., 1996; *Sutherland et al*., 2012]. The light source was an electroluminescent panel, which had maximum emission in the blue part of the visible spectrum. This source was placed behind the channel, 20 cm from the tank wall and midway along the channel (green dashed box in Figure 1). A Nikon D300 camera with a 200 mm Nikkor lens was fixed 6 m away from the channel. The camera was carefully levelled at the height of the water surface. Two grids on opposite sidewalls of the tank, were used to ensure that the camera optical axis was perpendicular to the tank walls. The setup was designed to minimize parallax errors and image distortions. Camera exposure and white balance were set to maximize the camera sensitivity and a shutter speed of 0.2 s was sufficient to allow instantaneous images of the flow field. Picture resolution was 12 Megapixels, corresponding to a spatial resolution in the channel of 0.2 mm. Images were recorded in RAW format, and postprocessed with "RawPictureProcessor."

The Beer-Lambert law was applied to each pixel in the digital photographs. This law expresses a linear relationship between the concentration c of a dissolved substance and its attenuation of light $A=\log(I_0/I)$ at a given wavelength and along a given optical path, according to the formula

$$A=\epsilon_{abs}lc. \tag{2}$$

Here I_0 and I are the intensities measured at a given wavelength from an image with no dye and from images taken during the experiment, respectively, ϵ_{abs} is the molar attenuation coefficient and l is the path length through the water. I_0 was not measured directly as there was always dye in the channel. Instead, a reference image was taken of a uniform dye concentration produced by completely mixing the water manually after each experiment. The corresponding intensity I_{ref} is measured and used as a reference for the attenuation. Hence we use the quantity $A^*=A-A_{ref}=\log(I_{ref}/I)$ to calculate density, where $A_{ref}=\log(I_0/I_{ref})$. The blue component of the images was used, as this part of the visible spectrum is most strongly absorbed by the red dye and hence gives the highest sensitivity.

A calibration carried out before the experiments determined the range of validity of the linear relation (equation (2)) and the maximum dye concentration was chosen to lie within this linear response. Thus the mean dye concentration (and hence salt concentration) along the ray path is proportional to the attenuation A^* at any point of the flow. Effects of light refraction by the largest density gradients were tested and contributed to only sub-millimetre offsets of the apparent vertical position of measurements, and were therefore neglected. A linear extrapolation was necessary within millimetres of the bottom and top of the measurement area in order to correct for internal reflections from the tank bottom and the water surface.

Before each experiment, water samples were taken using syringes fixed at the bottom of the tank and just below the free surface of the water. The density of each sample was measured to ± 0.01 kg m^{-3} using an AntonPaar densimeter, providing a two-point calibration for the density fields obtained from the light attenuation method.

The technique was carefully validated by comparing density profiles inferred from light absorption and densitymeter measurements at the beginning and after 20 ridge transits. The profiles matched very well even at the bottom of the mixed layer where density/dye concentration gradients are the largest as shown in Figure 2 (a). Estimated vertical error bars due to the sampling method are shown in Figure 2b, from which we see that the two techniques are consistent at the sampled depths within the uncertainty. The molecular diffusion of dye was tested by leaving the stratified channel with no forced flow for 20 hrs. In this case, density

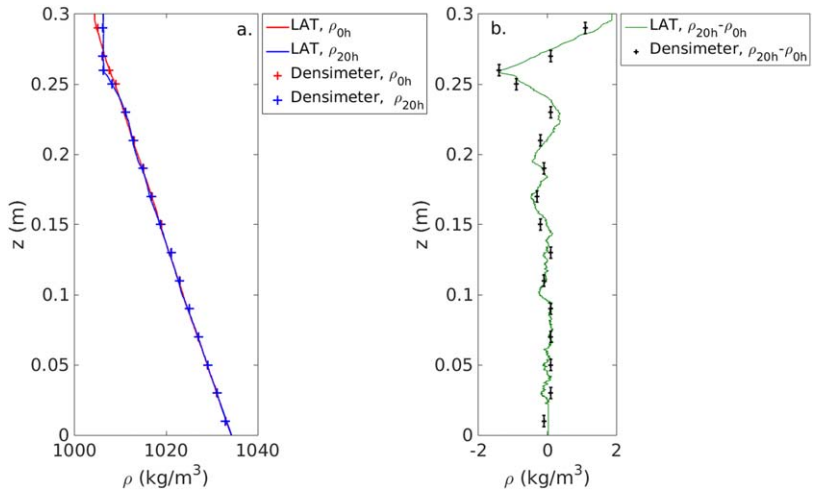

Figure 2. (a) Comparison of density profiles obtained from light attenuation technique (solid lines) and densimeter measurements (crosses) in exp21. (b) Density difference between initial and final states from light attenuation technique (solid line) and densimeter measurements (black error bars).

changes were negligible apart from a slight weakening of the gradient within 2 mm of the free surface and of the channel base.

The light attenuation technique produced instantaneous, full-field density measurements $\rho_{inst}(x, z, t)$ averaged along the optical path through the width of the channel (where t is time). The method also allowed accurate measurement of the vertical density profile, in particular at times of no motion. Further accuracy was achieved by horizontal averaging in x across the field of view to give $\bar{\rho}(z)$. From the differences between the rest state density profiles before and after each transit of the ridge we calculated the amount of irreversible mixing caused by each transit.

The light attenuation technique captures the integrated density anomalies along an optical path and as a consequence does not provide reliable quantitative information on the dimensions of three dimensional structures at the overturning scales. On the other hand, refractive index variations visible on the shadowgraph images indicate the extent (normal to the light path) of the turbulent structures.

2.3. Experiments

Two types of experiment were carried out; we term these single-tow and multiple-tow. In the single-tow experiments the upstream stratification was characterized by a uniform buoyancy frequency produced by the filling technique. Density fields were measured before, during and after a single transit of the ridge, and shadowgraph images were taken for visualization of the turbulence.

The magnitude of restratification processes in regions of rough, small scale topographies is poorly known. Multiple tows experiments permit to describe the dynamics of mixing in a range of stratifications relevant to model the ocean stratification upstream of topographic features. In multiple-tow experiments the ridge was towed back and forth along the length of the channel 20 times over 20 hrs. After each transit the water was left to come to a resting state for 1 hr prior to the next ridge transit (visible motion ceased after approximately 20 minutes). Photographs for the light attenuation measurements were taken at 5 minute intervals over the entire course of the experiment and later processed to obtain 300 density fields. During each ridge transit (and shortly afterward), a number of shadowgraph photographs were also taken. The multiple-tow experiments enabled measurements of the mixing induced by each transit as well as the accumulated mixing over n transits. They also revealed changes in the location of the mixing as the upstream stratification evolved from the initial uniform buoyancy frequency (the first ridge transit, equivalent to the single-tow experiments) into a well-mixed boundary layer and pycnocline structure. We propose that such a stratification is more likely to represent oceanic conditions, although the rate of restratification processes in regions of rough, small scale topographies is poorly constrained. Multiple tow experiments therefore provided estimates of the mixing rate for a range of stratifications potentially relevant to the ocean stratification upstream of topographic features.

Table 1. Listing of Parameters Used in All Experiments[a]

Experiment	Ridge Width (cm)	N_0 (rad/s)	U (cm/s)	Fr_h	Fr_L	Re
exp*A*	5	1.00	0.9	0.2	0.2	430
exp*B*	5	1.00	3.4	0.9	0.7	1700
exp*C*	5	1.00	7.0	1.7	1.4	3500
exp*D*	5	1.00	17.3	4.3	3.5	8700
exp*E*	5	1.00	34.8	8.7	7.0	17000
exp01	5	0.46	1.7	0.9	0.7	870
exp13*	5	1.34	8.7	1.6	1.3	4400
exp11*	5	1.20	8.7	1.8	1.4	4400
exp03	5	1.01	8.7	2.1	1.7	4400
exp15*	5	1.36	17.4	3.2	2.6	8700
exp06*	5	0.99	17.3	4.3	3.5	8700
exp07	5	1.00	17.3	4.3	3.5	8700
exp21	5	0.99	43.4	11.0	8.8	22000
exp17	5	1.01	174.0	43.9	34.0	87000
exp28	16	0.98	1.7	0.44	0.1	1700
exp30	16	0.98	3.5	0.88	0.2	3500
exp31	16	1.00	7.0	1.7	0.4	7000
exp32	16	0.95	7.0	1.8	0.4	7000
exp36	16	1.13	7.8	1.7	0.5	7800

[a]Star labels indicate experiments for which the initial stratification is partially mixed owing to a previous experiment run in the same fill.

The relevant flow parameters are the vertical Froude number (based on ridge height, $Fr_h \equiv U/(N_0 h_0)$), the lateral Froude number ($Fr_L \equiv U/(N_0 l_r)$) and the Reynolds number ($Re \equiv U l_r/\nu$), where l_r is the scale of the largest turbulent structures and ν is the kinematic viscosity of water. The vertical Froude number is the inverse of the steepness parameter, ϵ, defined by *Nikurashin and Ferrari* [2010a]. Linear lee waves can occur when $Fr_h > O(1)$; at smaller values of Fr_h nonlinear processes such as blocking and low-level breaking occur [*Baines and Hoinka*, 1985; *Winters and Armi*, 2014]. In this paper we refer to this regime as the nonlinear regime, where the nonlinearity relates to the flow regime, rather than the emitted lee waves. The lateral Froude number is the dimensionless frequency of lee waves and equivalent to the parameter χ defined by *Nikurashin and Ferrari* [2010a]. For significant radiation of waves, $Fr_L < O(1)$ is required, implying that for larger values of Fr_L energy and mixing is trapped close to topography. The Reynolds number dictates the likelihood of local turbulence. The laboratory experiments have smaller Re than the ocean (although usually much larger than three-dimensional numerical simulations) and our goal is to look for results showing asymptotic behaviour at large Re that can be used to infer oceanic behaviour.

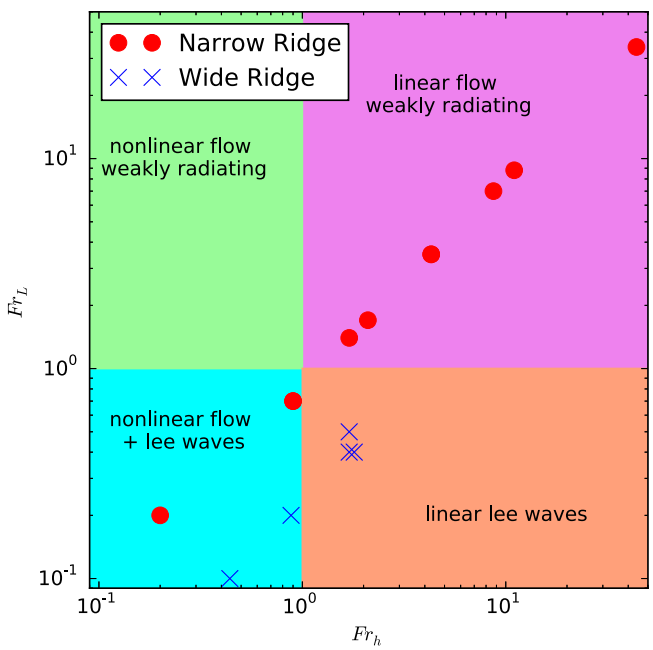

Figure 3. Experimental conditions for the two ridges in Froude number space and dynamical regimes.

The experiments (Table 1) were designed to span multiple parameter regimes, as shown in Figure 3, despite limitations from ridge and channel lengths and Reynolds number. For clarity, the delineation between parameter regimes are shown as distinct boundaries in the diagram, however it is expected that the evolution of the flow dynamics with Fr_h and Fr_l are gradual. For a given ridge width the two Froude numbers are proportional to each other. We highlight a number of experiments in the nonlinear flow regime (lower left quadrant). Only the wider ridge broaches into the linear lee wave regime. Cases with larger velocity (and larger Reynolds

numbers) tend toward the weakly radiating regime, where vertical oscillations induced by the topography have a primary frequency too high to be able to efficiently radiate as internal waves (although, in practise, a limited range of topographic wavenumbers smaller than N/U is generated by the Gaussian topography, so that a finite contribution to the energy flux into lee waves is possible.)

2.4. Irreversible Mixing

The amount of mixing is defined in terms of changes in gravitational potential energy, and we adopt the physical framework of *Winters et al.* [1995]. For a density field $\rho(x,z,t)$ in a volume V with horizontal area A_b the potential energy per unit horizontal area is

$$PE(t)=(g/A_b)\int_V \rho(x,z,t)z\mathrm{d}V. \tag{3}$$

This potential energy is partitioned between the background potential energy *BPE* (the minimum potential energy that can be reached through an adiabatic sorting of the density field) and the remainder, which can lead to motion and hence is the available potential energy $APE=PE-BPE$. The density field can be similarly expressed as $\rho(x,z,t)=\bar{\rho}(z,t)+\rho'(x,z,t)$, where $\bar{\rho}(z,t)$ is the background density profile and $\rho'(x,z,t)$ is the density anomaly associated with fluid motions. By construction, the background density profile and potential energy can only change through diabatic processes such as irreversible mixing. In the present experiments the flow reaches a state of no motion approximately 20 minutes after forcing is stopped at the end of each transit. In this state the background potential energy per unit horizontal area is simply expressed as

$$BPE(i)=PE(i)=g/A_b\int_0^H \bar{\rho}_i(z)z\mathrm{d}z, \tag{4}$$

where $\bar{\rho}_i$ is the background density profile after the i-th transit. The difference

$$\Delta BPE(i)=BPE(i)-BPE_0 \tag{5}$$

is the accumulated amount of irreversible mixing induced by the flow over i transits of the ridge.

3. Results

3.1. Flow Dynamics

In this section we describe the flow when the ridge was towed once through a linear stratification for a range of parameters. Mixing is identified by regions of turbulence, indicated by active, small-scale refractive index gradients in shadowgraph images, while instantaneous density measurements reveal the wave field. We use the terms upstream and downstream to refer to the flow in the ridge reference frame. We remind the reader that, with the inverted ridge at the top of tank, topographically induced density perturbations are of the opposite sign to those in the ocean.

3.1.1. Nonlinear Regime

In exp*A* (Table 1) a small ridge speed corresponds to a small vertical Froude number, $Fr_h=0.2$, and we identify upstream blocking and lee waves (Figure 4, top row). There is a quiescent region upstream of the ridge over the whole depth, associated with a negative density anomaly between $z=0.25$ m to $z=0.30$ m caused by less dense water being forced downward by the ridge motion. Radiation of waves ahead of the moving ridge create a negative density anomaly in the upstream region [*Browand and Winant*, 1972; *Baines*, 1988]. A turbulent patch, identified by fine-scale structures in the shadowgraph image, is formed in the wake of the ridge and has a vertical extent comparable with the ridge height. A strong positive density anomaly is measured at the core of the turbulent patch, indicating upward displacement of isopycnals and an upward component of motion in the lee of the ridge. A vertically periodic structure of alternating positive and negative density anomalies is radiated into the underlying stratification ($z=0$ to $z=0.25$ m), corresponding to the vertical propagation of steady internal lee waves with a vertical wavelength of 65 $\pm$2 mm. This vertical wavelength matches the wavelength of lee waves predicted by *Klymak et al.* [2010]:

$$\lambda=\frac{2\pi UH}{(H-h_0)N}=68\pm1\ \mathrm{mm}. \tag{6}$$

Interference due to wave reflection at the tank bottom are observed downstream, but there is no indication of mixing in the lower region.

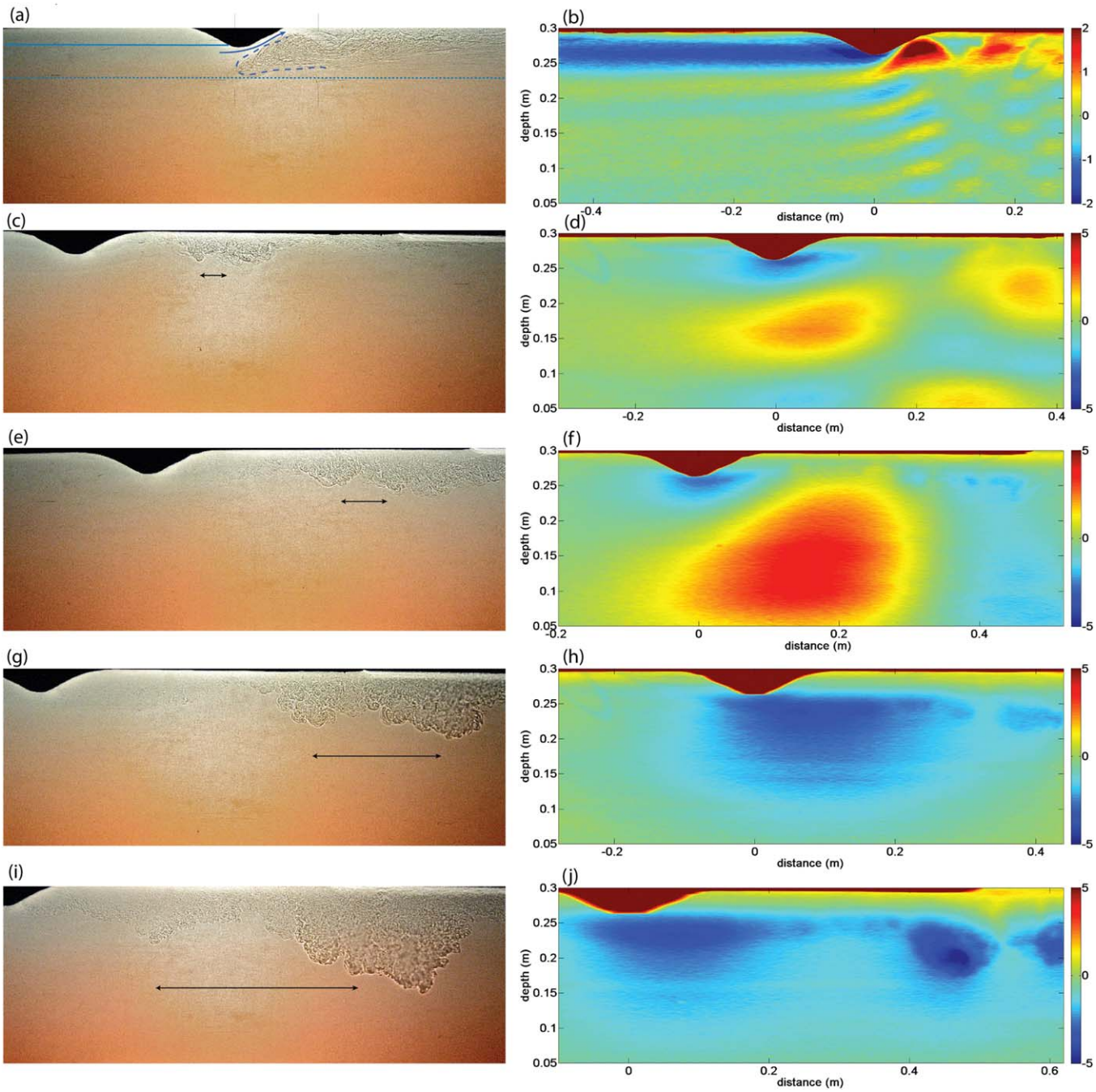

Figure 4. Single tow experiments with the narrower ridge, showing shadowgraph images (left column) and density perturbations (right). (a, b) ExpA and (c, d) exp*B* have small vertical Froude number (nonlinear flow regime); (e, f) exp*C*, (g, h) exp*D* and (i, j) exp*E* are all in the linear, weakly radiating regime. The double arrow shows the characteristic lengthscale of buoyant motions $U/N * h/L$. In the top left panel the solid blue line, the arrow, the dashed line and the dotted line respectively indicate the blocking region, the jet, the stagnant region and the separation from the uncoupled flow, described by *Winters and Armi* [2014].

The dynamics in this experiment is similar to stratified flow over a ridge in the small vertical Froude number regime described in recent numerical simulations [*Klymak et al*., 2010; *Winters and Armi*, 2014]. The flow is characterized by a blocking region upstream of the ridge and an accelerated jet-like layer forming over the ridge crest. This jet is isolated from the outer stratified flow by a stagnant region of uniform density [*Winters and Armi*, 2014]. As the jet accelerates, strong shear instabilities can be induced in the boundary layer [*Winters and Armi*, 2013], generating irreversible mixing of the background stratification, as observed downstream in exp*A*. Despite being well outside the linear wave regime, radiating lee waves are clearly present

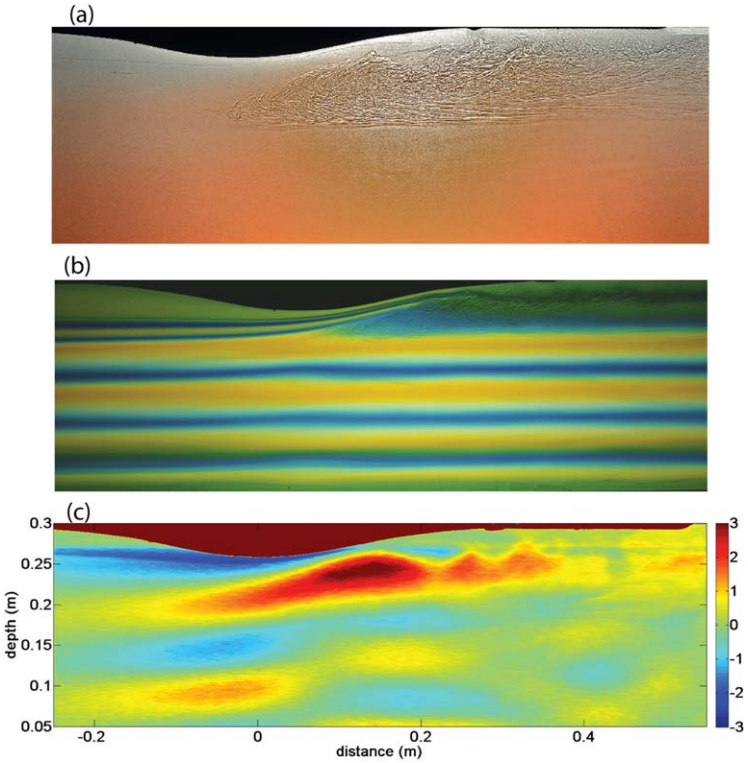

Figure 5. (a) Shadowgraph; (b) dyed isopycnal layers and (c) density perturbations for flow over the wider ridge at $Fr_h = 0.44$, $Re = 1700$ (exp28).

as predicted in the numerical simulations of *Klymak et al.* [2010], but do not produce visible signs of turbulent mixing.

3.1.2. Weakly Radiating Regime

As the ridge velocity is progressively increased (exp*A* – *E*, Table 1) the conditions shift toward the linear regime (larger Fr_h), while simultaneously shutting off radiating waves (larger Fr_L; i.e., moving toward the top-right quadrant of Figure 3). Reynolds number is also increased. Comparing exp*B* with exp*A* (Figure 4, top and second rows) the accelerated jet over the ridge narrows and a centimeter-scale turbulent layer is seen on the downstream slope of the ridge. In the wake of the ridge a turbulent patch develops, measuring 50 mm in the vertical and 150 mm in the horizontal. Generation of internal lee waves occurs downstream, with a typical vertical wavelength of 20 cm, close to the wavelength of 25 cm predicted by *Klymak et al.* [2010] in a regime of $Fr_h \ll 1$.

At still larger Fr_h (exp*C*; Figure 4, third row) the turbulent patch develops further downstream from the ridge and is larger in its vertical extent. Despite conditions being outside the radiation regime, the density anomalies are consistent with lee waves that have a vertical wavelength limited by the water depth. With further increases in ridge velocity (Figure 4, bottom two rows) lee wave propagation ceases, spatial variations in the turbulent wake region become more prominent and turbulence penetrates deeper into the water column. In particular, turbulent bursts periodically penetrate downward. The periodic generation of turbulent bursts at large Fr_h can be qualitatively explained.

After passing over the ridge, fluid parcels move toward the ridge base (as seen in the density field) and start to oscillate at the buoyancy frequency N_0. The theoretical oscillation magnitude is larger than h, however the fluid parcels oscillation is impeded by the ridge boundary, leading to strong local velocity gradients. The induced shear instability generates regions of more intense mixing once each buoyancy period. In these experiments with a towed ridge, the typical distance between subsequent bursts scales with the expected characteristic horizontal lengthscale $U/N_0 \cdot h_0/L$ of buoyancy oscillations (double arrows in Figure 4) [*Klymak et al.*, 2010].

3.1.3. Linear Lee Wave Regime

Experiments with the wider ridge provide cases having $Fr_h > Fr_L$, thereby accessing conditions in which linear lee waves can occur (i.e., $Fr_h > O(1)$; $Fr_L < O(1)$; lower-right quadrant in Figure 3). Figure 5 (exp 28) shows the nonlinear regime for this wider ridge, where again there is blocking, hydraulically controlled flow, an accelerated jet over the ridge that extends far upstream, a mixed relatively uniform density region downstream that extends into the oncoming flow above the crest of the ridge, and lee wave radiation. At $Fr_h \approx 1$ (Figure 6, exp30) the upstream blocking persists and lee waves have vertical wavelengths comparable to the ridge width. In this case the dye layers marking isopycnals show mixing at around three ridge heights, possibly due to partial wave overturning. In fact, the parameters $Fr_h = 0.88$ and $Fr_L = 0.2$ and the flow dynamics are consistent with the wave overturning regime described in the analytical approach of *Muraki* [2011] (their Figure 4). The observed mixing is relatively weak and is not visible in shadowgraphs.

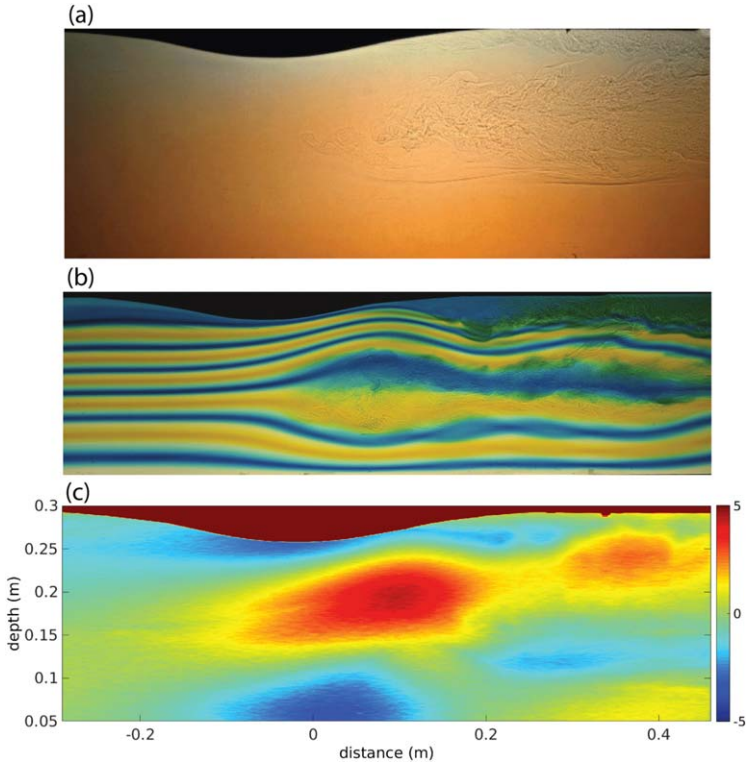

Figure 6. (a) Shadowgraph; (b) dyed isopycnal layers, and (c) density perturbations for flow over the wider ridge at $Fr_h = 0.88$, $Re = 3500$ (exp30).

At larger velocities (Figure 7, exp32) the blocking effects disappear. Long wavelength lee waves, as well as intense mixing in the downstream wake, persist. There are no indications of mixing remote from the topography. We highlight the similarities between exp32 (Figure 7) and expC (Figure 4, third row). The strong similarities in the dynamics for the two ridge widths suggest that the mixing is primarily controlled by the vertical Froude number Fr_h. In both cases, the qualitative observations suggest that mixing is dominated by the turbulent wake region.

3.1.4. Summary

The qualitative results of these experiments are broadly consistent with the regime diagram of Figure 3. We are able to access three different parameter regimes, including the linear quasi-steady lee wave regime. However, the transition between these regimes is gradual. We now look to quantify the irreversible mixing that occurs in each regime.

3.2. Irreversible Mixing

In the multiple-tow experiments the rest state vertical density profiles are found from the density fields during the 1 hr pause between ridge transits. We recall that the ridge was towed once every hour, and density fields were recorded every five minutes. The density profiles are then used to evaluate the irreversible mixing during each ridge transit.

Examples of the evolution of the density profile (after subtracting the initial density profile and normalizing by the initial top-bottom density difference) is shown in Figure 8 for five multiple-tow experiments with a range of ridge speeds. After the first transit the water is partially mixed to a depth comparable to the ridge height, resulting in a region of increased density close to the surface and a region of decreased density immediately below. After several transits a thoroughly mixed layer has formed and it gradually deepens during subsequent transits (e.g., at a rate $0.02h_0$ per transit in exp07). The depth and magnitude of density changes in the mixed layer increase with ridge speed: for example, the mixed region formed after 20 transits is similar to the ridge height h_0 in exp01 (Figure 8a) and is $4h_0$ in exp17 (Figure 8e); the corresponding maximum normalized density changes in the mixed layer are $\pm 1\%$ and $\pm 20\%$. Changes in density due to irreversible mixing at depths greater than $4h_0$ are very small in all of the experiments.

For each multiple-tow experiment the value of ΔBPE (equation (5)) is calculated for each rest period between transits (Figure 9), using the average of the density profiles during the state of no motion after each transit. For the nonlinear flow regime (exp01, cyan line in Figure 9a) a relatively small change of ΔBPE is found, reaching an accumulated increase of just 5×10^{-3} J m^{-2} after the ninth pass. The weak mixing in this experiment is likely due to the very low Reynolds number; such a low Reynolds number makes this experiment a poor approximation to the ocean and we therefore don't include this experiment in the detailed analyses below.

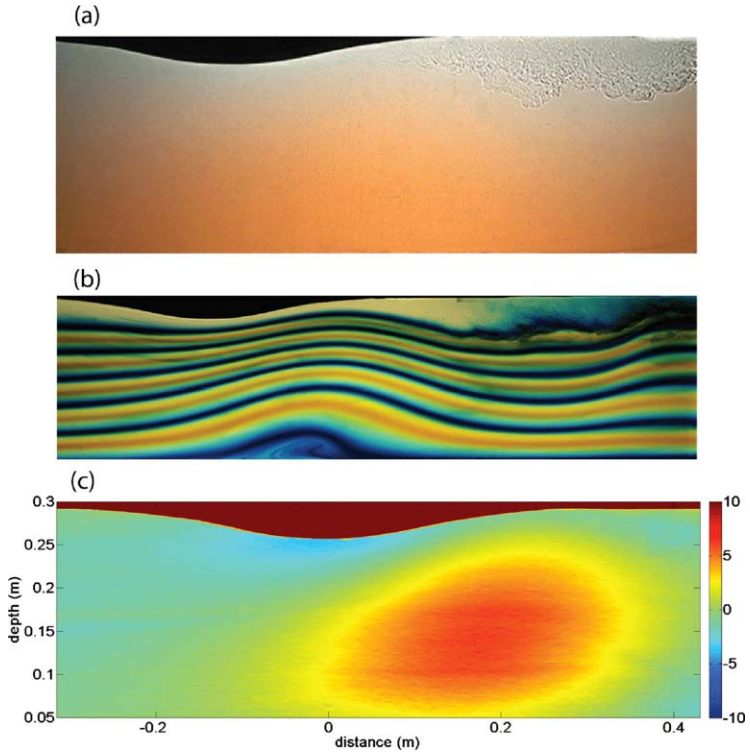

Figure 7. (a) Shadowgraph; (b) dyed isopycnal layers, and (c) density perturbations for flow over the wider ridge at $Fr_h = 1.8$, $Re = 7000$ (exp32).

In the weakly radiating regime at larger Fr_h (magenta lines in Figure 9a) ΔBPE shows substantial increases, monotonic with transit number, consistent with the irreversible transfer of energy toward *BPE* by mixing. The first transit produces the largest jump in ΔBPE. This jump scales with Fr_h (red circles in Figure 10a). Once a mixed layer develops (initially to the height of the ridge crest) it progressively deepens with subsequent ridge transits, ΔBPE continues to increase linearly with transit number (red circles in Figure 10b). The rate of mixing from later transits is weakly dependent on Fr_h.

A similar dependence on Froude number and on upstream density structure is found with the wider ridge (Figure 9b), both in the nonlinear flow (cyan lines) and linear lee wave (orange lines) regimes. Again mixing is largest when the upstream flow is uniformly stratified: the first ridge transit gives $\Delta BPE \approx 0.01$ to 0.03 J m^{-2}, which is larger than that for the narrower ridge at a given Fr_h (blue crosses in Figure 10a). After the formation of the mixed layer with a strong underlying pycnocline, ΔBPE again continues to rise at a constant rate for subsequent transits; this rate again depends on Fr_h but is now smaller than (approximately one third of) that for the narrower ridge ($0.8\times10^{-3}-2.3\times10^{-3}$ J m^{-2} transit^{-1}; blue crosses in Figure 10b). It will be shown below that most of the mixing after the first few transits occurs through deepening of the mixed layer rather than by internal wave activity.

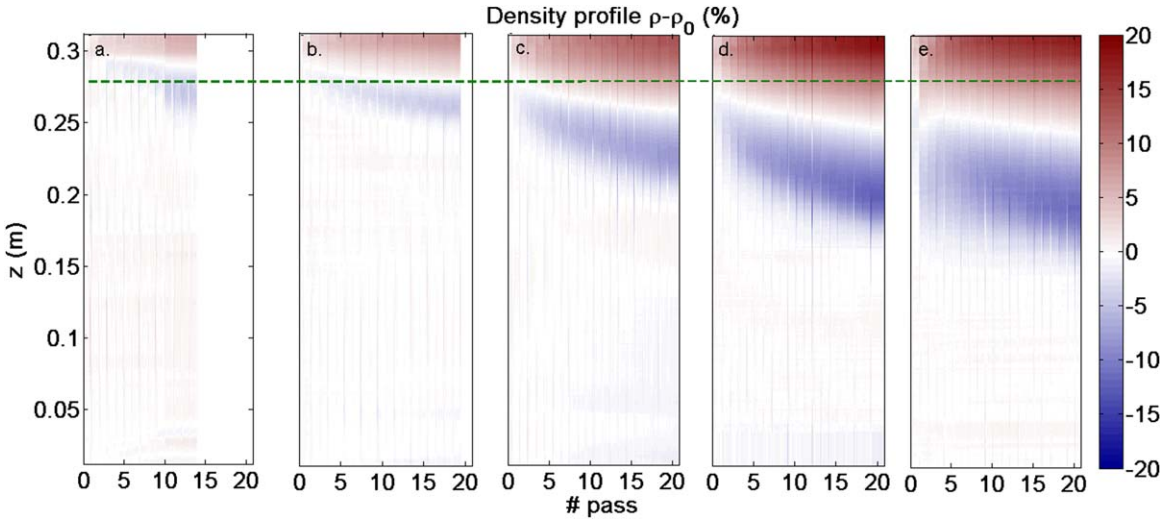

Figure 8. Time series of the horizontally averaged density profile differenced from the initial density profile $\rho_0(z)$ and expressed as a percentage of the initial density difference $\rho_{bottom}-\rho_{top}$: (a) exp01, (b) exp03, (c) exp07, (d) exp21, and (e) exp17. Twelve density fields were obtained in each pause between ridge transits. The regularly spaced vertical stripes correspond to density measurements immediately after a ridge transit and before the water was at rest. The green dashed line shows the depth of the ridge crest.

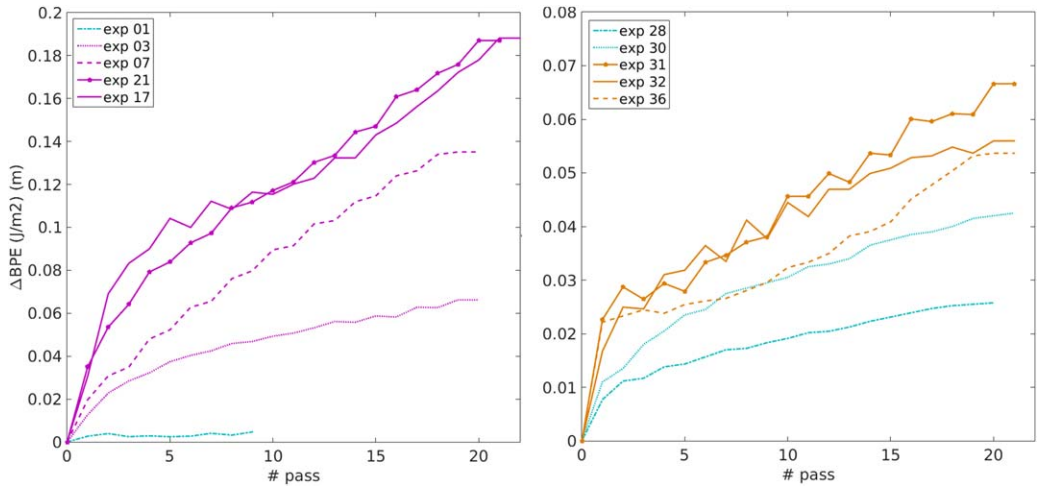

Figure 9. The evolution of background potential energy averaged over each rest period between ridge transits for (a) five experiments with the narrow ridge and (b) five experiments with the wide ridge. Line colour indicates the expected flow regime as in Figure 3: cyan for nonlinear flow, magenta for the weakly radiating regime and orange for linear lee waves.

3.3. Depth-Dependence of Mixing

The measured irreversible mixing is heterogeneously distributed over the water depth, particularly following the development of the near-topographic mixed layer, after which most mixing is located at the pycnocline. However, quantification of the energy lost to mixing using BPE relies upon density changes integrating to zero; thus, the relative amount of irreversible mixing in different parts of the domain cannot be quantified. For this reason, we analyze the vertical variations in vertical mixing using the total flux of density, $F_\rho(z)$, defined such that

$$\frac{\Delta\bar{\rho}}{\Delta t} = \frac{\partial F_\rho}{\partial z}, \tag{7}$$

where $\Delta\bar{\rho}$ is the difference in average density profiles between two quiescent periods (before and after a series of obstacle tows) and Δt the timescale associated with the tow. Upon vertical integration from the floor of tank (where F_ρ is zero) to a level z, we find

$$F_\rho(z) \propto \int_0^z \Delta\bar{\rho}\, dz. \tag{8}$$

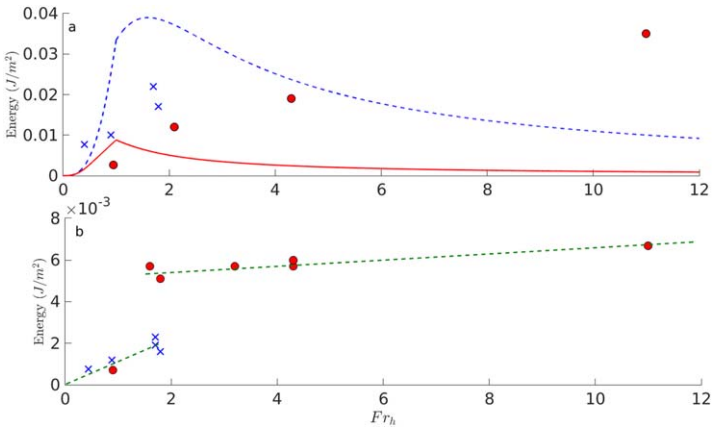

Figure 10. The measured *BPE* change as a function of vertical Froude number for (a) the first ridge transit and (b) the average ΔBPE per transit after five transits for the narrower (circles) and wider (x) ridges. Lines in Figure 10a show the predicted energy input to linear lee waves during a single pass with uniform buoyancy frequency upstream, for the narrower (solid) and wider (dashed) ridges. Dashed lines in (b) show ΔBPE trends at lower and larger Fr_h. The supplementary data points in Figure 10b) correspond to experiments performed in a partially mixed initial stratification.

Thus, for an initially linear density profile, an assumption that vertical flux behaves like a diffusive process (i.e., $F_\rho \sim K_\rho \frac{\partial \rho}{\partial z}$) implies that the cumulative density difference is proportional to the turbulent diffusivity of density, K_ρ.

To estimate the vertical distribution of mixing we normalize the vertical flux of density relative to its maximum value, and plot profiles vertical flux estimated from the first twelve transits of each experiment (Figure 11). In all cases mixing in the interior is weaker than the near-topography region. In the nonlinear flow regime (cyan lines) there is strong

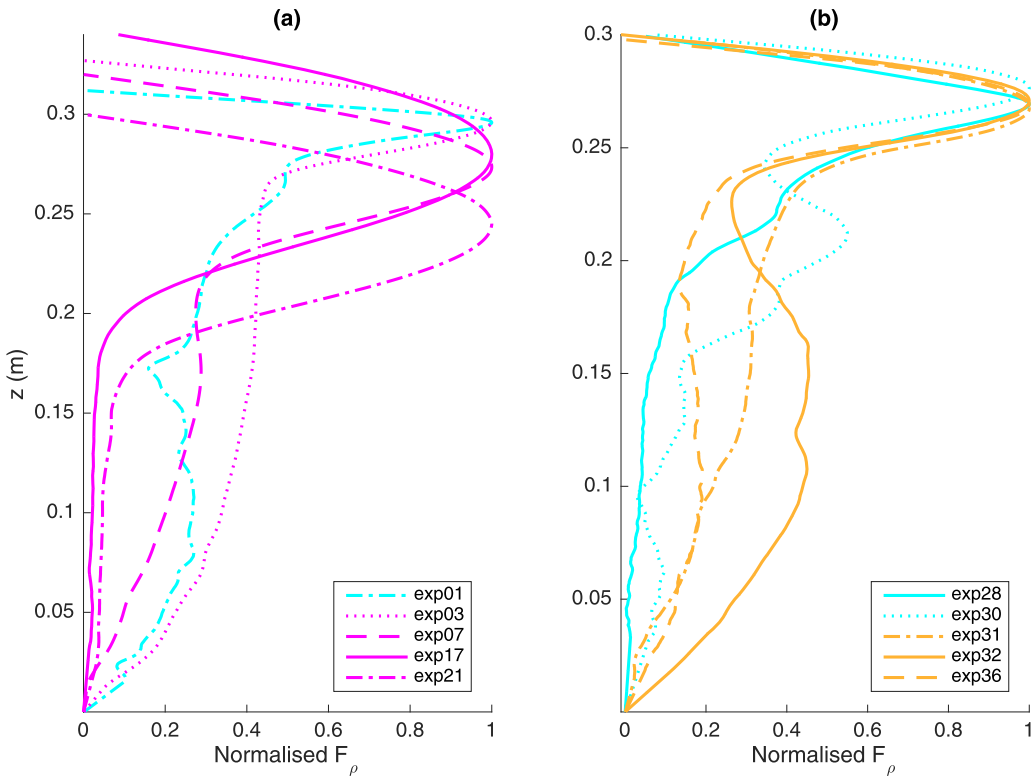

Figure 11. Normalized vertical density flux calculated from first 12 transits, as per equation (8) for (a) Narrow and (b) wide ridge. Line colour indicates the expected flow regime as in Figure 3: cyan for nonlinear flow, magenta for the weakly radiating regime and orange for linear lee waves.

mixing above $z \approx 0.25$ m (within $\sim 1.5h_0$ of the surface), while mixing at middepth is between 10% and 30% of the near-topography mixing. On the other hand, in the linear lee wave regime (orange lines) the profiles show a larger percentage of mixing is broadly distributed in the deep stratified region, while the strongest mixing remains localized near the topography (within $\sim 2h_0$ of the surface). Experiments in the weakly radiating regime (magenta lines) show wake mixing that progressively deepens with Froude number; deeper mixed layers correlate with reductions in the interior density flux.

Thus the vertical location of density differences confirm that irreversible mixing occurs primarily in the vicinity of the ridge, where turbulence was observed. The radiation of lee waves readily observed in the density field measurements corresponds to only a relatively small rate of mixing at larger depths.

4. Discussion

4.1. Comparison of Volume-Integrated Mixing With Linear Wave Theory

For the purposes of allowing the vertical diffusion in ocean models to be dynamically responsive it is currently necessary to parameterize the energy input into the lee waves produced by bottom topography and the mixing rates associated with dissipation of that energy [*Nikurashin and Ferrari*, 2013, and references therein]. The energy input to radiating internal waves has been estimated from linear theory [*Bell*, 1975], which applies for subcritical flow over two-dimensional topography ($Fr_h > 1$), small wave frequencies ($Fr_L < 1$), and the limit $h_0 \ll H$, where H is the water depth. In the present experiments the water depth was chosen such that $H/h_0 \sim 8.6$ and is comparable to the depth ratios of most interest in the oceans, where a 500 m ridge on the abyssal plane has $H/h_0 \approx 8$. Hence it is assumed that the rates of local mixing are likely to be insensitive to water depth and we therefore compare with linear theory for infinite water depth. However, we note that wave reflection from the surface could potentially enhance mixing (a process that may also occur in the ocean).

For the analytical ridge shapes (equation (1)) used in the experiments, the energy flux E_f to linear internal waves is given by [Bell, 1975]

$$E_f = \frac{\rho_0 U}{2\pi} \int_0^{N/U} P(k)(N^2 - U^2k^2)^{1/2} Uk dk, \tag{9}$$

with k and $P(k)$ the wavenumber and topography spectrum, respectively. The background stratification in our case is $N = 1$ rad s^{-1}. The total energy input to waves during a single ridge transit along the channel of length L becomes $E_{in} = E_f * L/U$. Saturation of energy flux in the nonlinear regime ($Fr_h < 1$) is accounted for by multiplying the energy input by Fr_h^2 [*Nikurashin and Ferrari*, 2011].

The predicted linear flux is superimposed in Figure 10a for comparison with the measured *BPE* increase for the first ridge transit. The predicted input for the wider ridge is a factor of four larger than that for the narrower ridge. For $Fr_h \ll 1$ a large range of wavenumbers contribute to the predicted input to lee waves and the energy input is relatively small. For $Fr_h \gg 1$ linear waves carry more energy, but only a limited range of wavenumbers can propagate. In both these limits the total energy input can be an order of magnitude smaller than the maximum value, which is reached at $Fr_h \approx 1$.

The measured change in BPE due to mixing exceeds the predicted lee wave radiation for cases exp03, exp07 exp21 and exp28, while mixing is within 50% of the predicted radiation in the other four cases. Recall that only a fraction of the radiated energy input is expected to contribute to irreversible mixing. While a mixing efficiency $\bar{\Gamma} \approx 0.5$ for the wider ridge might be feasible, $\bar{\Gamma} \geq 1$ is not possible. We therefore conclude that energy input to linear lee waves cannot produce the measured mixing at $Fr_h > 1$ (in the weakly radiating regime) and that the mixing includes substantial contributions from other mechanisms.

The *BPE* increase after the first five transits of the ridge (i.e., once a mixed layer has formed) is shown in Figure 10b. For the experiments with the wider ridge, performed at $Fr_h \leq 2$, a linear trend for the evolution of ΔBPE with Fr_h is observed. It can be expressed as $\Delta BPE \propto Fr_h$, with a constant of proportionality of $O(10^{-3})$J m^{-2}. The time available for mixing is proportional to the transit time $\Delta t \propto L/U$, and the average rate of mixing expresses as

$$\frac{\Delta BPE}{\Delta t} \propto \frac{Fr_h U}{L} = \frac{U^2}{NhL}. \tag{10}$$

Hence, the mixing rate is proportional to the kinetic energy available in the flow in the $Fr_h \leq 2$ regime. It is also inversely proportional to N, which indicates that stronger stratification below the mixed layer inhibits mixing. Thus, in situations where topographically induced mixing is sufficiently rapid to prevent restratification of the near-topography mixed layer, the interior mixing due to lee waves will likely be reduced.

The narrow ridge gave approximately twice the amount of mixing at $Fr_h \approx 2$ (in the later transits). For larger vertical Froude numbers the average ΔBPE does not vary substantially. Consequently, the mixing rate increases linearly with the flow momentum:

$$\frac{\Delta BPE}{\Delta t} \propto \frac{U}{L}. \tag{11}$$

At the ocean scale, these results may help to anticipate the behavior of mixing rates in terms of Fr_h. For $Fr_h \leq 2$, variations of the mixing rate as Fr_h^2 can be expected, while variations as Fr_h are expected for $Fr_h \geq 2$.

4.2. Evaluation of Near-Topographic Mixing

The experimental results provide constraints on the vertical partitioning of mixing and energy dissipation. The relative contribution of near-topography mixing (caused primarily by turbulent flow generated in the wake of the topography) was visually observed to be stronger than remote mixing (induced by radiated internal wave energy). We now look to quantify these differences as a function of flow regime.

The fraction of mixing that occurs near topography can be assessed by quantifying two different parameters from the experiments. The first parameter is the depth of the layer, h_m, over which mixing is intensified. In each experiment the maximum value of normalized density flux (see Figure 11) occurs close to topography, and then decreases. We define the vertical location of maximum mixing, z_m, and then calculate the nondimensional mixed layer depth as

$$h_m \equiv \frac{2(H - z_m)}{h_0}$$

Values of h_m as a function of horizontal Froude number are plotted in Figure 12a. In the narrow ridge cases (red circles) we see a clear trend of increasing mixed layer depth with Froude number as the flow moves

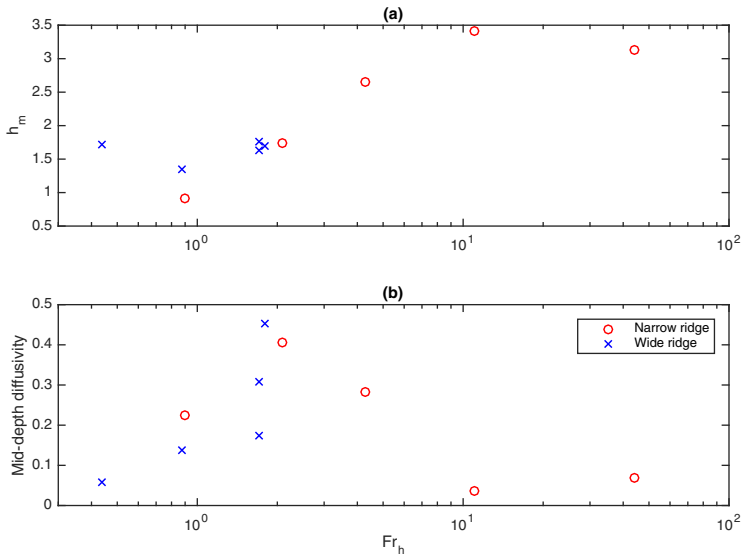

Figure 12. (a) Nondimensional mixed layer depth, h_m; and (b) normalized middepth diffusivity as a function of Froude number for the narrow (circles) and wide (x) ridges.

into the weakly radiating regime. At very small Froude numbers (the blocking regime), mixed layer depths are much smaller, with a minimum value at $Fr_h = 1$. There is a smooth transition between these cases.

The second metric to measure the relative importance of near-topographic mixing is the value of the normalized density flux at middepth (Figure 12b). In the low Froude number (topographic blocking) regime, very little mixing occurs outside the mixed layer region, especially in the wide ridge cases (noting that the small Reynolds number in exp01 makes it a questionable data point). In the linear lee wave regime, interior mixing is amplified, up to half the diffusivity of the mixed layer, but as Froude number increases into the weakly radiating regime, the interior mixing drops again. Thus, outside the band of Froude numbers at which linear lee wave radiation is significant, mixing occurs predominantly in the near-topography region.

The laboratory conditions span Froude numbers in the range [0.2, 40] and therefore include the oceanic values. At the laboratory Reynolds numbers, viscous effects that are not associated with the turbulent dissipation (particularly sidewall friction) may reduce the fraction of near-topographic mixing. For example, in experiments with interfacial wave breaking, it was found that the mixing efficiency was modified by only 2% when the viscous damping coefficient was doubled [*Hult et al.*, 2011a] at smaller *Re* (10^2, 10^3) than those in the present experiments. Hence we conclude that there are no obvious reasons why the relative contribution of local and remote mixing measured here should not be representative of oceanic flows over topography. Important caveats are that effects of irregular and three-dimensional ocean topography and the presence of inertial frequencies have not been investigated.

5. Conclusions

The results reported here provide the overall rate of irreversible mixing in stratified flow over two-dimensional topography at moderately large Reynolds numbers. At low vertical Froude number, the mixing increases with Fr_h, in proportion to the kinetic energy of the flow. In this nonlinear flow regime, hydraulic jumps and turbulent wakes behind the ridge dominate the mixing, meaning that most mixing occurs within one ridge height of topography. At intermediate values of vertical Froude number ($Fr_h \sim 1-2$) the total mixing continues to increase quadratically with velocity, but the resonance of forcing with low mode internal waves leads to radiation and remote mixing. At even larger ridge velocities, radiation is weakened and local mixing in a progressively deepening mixed layer dominates the flow; this result matches the expected weakly radiating regime.

The narrow range of resonance for the production of lee waves implies that lee waves may not be the dominant mechanism of mixing in the abyssal ocean. This result does not imply that the contribution of lee waves to remote mixing has been over-estimated. Indeed, the total mixing is much greater than that predicted by linear internal wave generation with physically plausible mixing efficiency. Thus, the local mixing due to flow-topography interactions may have been substantially under-estimated, and we advocate targeted studies to understand the full range of complex flow regimes possible. In particular, further work with

mixing due to the interactions of balanced flows with topography is warranted in order to assess the effects of inertial frequencies and complex, three-dimensional topography.

Acknowledgments
We thank Ben Tranter, Angus Rummery and Tony Beasley for technical support. Kraig Winters, Maxim Nikurashin and Callum Shakespeare are thanked for insightful discussions. The work was supported by the Australian Research Council grant DP120102744. GOH and AMH were supported by ARC Future Fellowships FT100100869 and FT120100842. The authors comply with AGU's data policy. The data used are listed in the references, tables and figures.

References

Allgayer, D. M., and G. R. Hunt (1991), On the application of the light-attenuation technique as a tool for non-intrusive buoyancy measurements, *Exp. Thermal Fluid Sci.*, *38*, 257–261.

Baines, P. G. (1988), A general method for determining upstream effectsin stratified flow of finite depth over long two-dimensional obstacle, *J. Fluid Mech.*, *188*, 1–22.

Baines, P. G., and K. P. Hoinka (1985), Stratified flow over two-dimensional topography in fluid of infinite depth: A laboratory simulation, *J. Atmos. Sci.*, *42*, 1614–1630.

Bell, T. H. (1975), Topographically generated internal waves in open ocean, *J. Geophys. Res.*, *80*, 320–327.

Bluteau, C. E., N. L. Jones, and G. N. Ivey (2013), Turbulent mixing efficiency at an energetic ocean site, *J. Geophys. Res. Oceans*, *118*, 4662–4672, doi:10.1002/jgrc.20292.

Browand, F. K., and C. D. Winant (1972), Blocking ahead of a cylinder moving in a stratified fluid: An experiment, *Geophys. Fluid Dyn.*, *4*, 29–53.

Bryden, H., and A. Nurser (2003), Effects of strait mixing on ocean stratification, *J. Phys. Oceanogr.*, *33*, 1870–1872.

Chalamalla, V. K., and S. Sarkar (2015), Mixing, dissipation rate, and their overturn-based estimates in a near-bottom turbulent flow driven by internal tides, *J. Phys. Oceanogr.*, *45*, 1969–1987, doi:10.1175/JPO-D-14-0057.1.

Davies Wykes, M. S., and S. B. Dalziel (2014), Efficient mixing in stratified flows: Experimental study of a Rayleigh-Taylor unstable interface within an otherwise stable stratification, *J. Fluid Mech.*, *756*, 1027–1057.

Eiff, O., F. Huteau, and J. Tolu (2005), High Reynolds-number orographic wave-breaking experiments, *Dyn. Atmos. Oceans*, *40*, 71–89.

Garner, S. T. (2005), A topographic drag closure built on an analytical base flux, *J. Atmos. Sci.*, *62*, 2302–2315.

Gayen, B., and S. Sarkar (2010), Turbulence during the generation of internal tide on a critical slope, *Phys. Rev. Lett.*, *104*, 218502.

Gheusi, F., J. Stein, and O. S. Eiff (2000), A numerical study of three-dimensional orographic gravity-wave breaking observed in a hydraulic tank, *J. Fluid Mech.*, *410*, 67–99.

Gregg, M. C., and E. Ozsoy (1999), Mixing on the black sea shelf north of the bosphorus, *Geophys. Res. Lett.*, *26*, 1869–1872.

Hacker, J., P. F. Linden, and S. B. Dalziel (1996), Mixing in lock-release gravity currents, *Dyn. Atmos. Oceans*, *24*, 183–195.

Hult, E. L., C. D. Troy, and J. R. Koseff (2011a), The mixing efficiency of interfacial waves breaking at a ridge: 1. overall mixing efficiency, *J. Geophys. Res.*, *116*, C02003, doi:10.1029/2010JC006485.

Hult, E. L., C. D. Troy, and J. R. Koseff (2011b), The mixing efficiency of interfacial waves breaking at a ridge: 2. local mixing processes, *J. Geophys. Res.*, *116*, C02004, doi:10.1029/2010JC006488.

Ivey, G. N., K. B. Winters, and J. R. Koseff (2008), Density stratification, turbulence, but how much mixing?, *Annu. Rev. Fluid Mech.*, *40*, 169–184.

Klymak, J. M., S. M. Legg, and R. Pinkel (2010), High-mode stationary waves in stratified flow over large obstacles, *J. Fluid Mech.*, *644*, 321–336.

Knigge, C., D. Etling, A. Paci, and O. Eiff (2010), Laboratory experiments on mountain-induced rotors, *Q. J. R. Meteorol. Soc.*, *136*, 442–450.

Lawrie, A. G. W., and S. B. Dalziel (2011), Rayleigh-Taylor mixing in an otherwise stable stratification, *J. Fluid Mech.*, *688*, 507–527.

Linden, P. F. (1979), Mixing in stratified fluids, *Geophys. Astrophys. Fluid Dyn.*, *13*, 3–23.

Melet, A., R. Hallberg, S. Legg, and M. Nikurashin (2014), Sensitivity of the ocean state to lee wave–driven mixing, *J. Phys. Oceanogr.*, *44*(3), 900–921, doi:10.1175/JPO-D-13-072.1.

Merzkirch, W. (1981), Density sensitive flow visualization, *Methods Exp. Phys.*, *18*, 345–403.

Munk, W., and C. Wunsch (1998), Abyssal recipes II: Energetics of tidal and wind mixing, *Deep Sea Res., Part I*, *45*(12), 1977–2010.

Muraki, D. J. (2011), Large-amplitude topographic waves in 2d stratified flow, *J. Fluid Mech.*, *681*, 173–192.

Nikurashin, M., and R. Ferrari (2010a), Radiation and dissipation of internal waves generated by geostrophic motions impinging on small-scale topography: Theory, *J. Phys. Oceanogr.*, *40*, 1055–1074.

Nikurashin, M., and R. Ferrari (2010b), Radiation and dissipation of internal waves generated by geostrophic motions impinging on small-scale topography: Application to the southern ocean, *J. Phys. Oceanogr.*, *40*, 2025–2042.

Nikurashin, M., and R. Ferrari (2011), Global energy conversion rate from geostrophic flows into internal lee waves in the deep ocean, *Geophys. Res. Lett.*, *38*, L08610, doi:10.1029/2011GL046576.

Nikurashin, M., and R. Ferrari (2013), Overturning circulation driven by breaking internal waves in the deep ocean, *Geophys. Res. Lett.*, *40*, 3133–3137, doi:10.1002/grl.50542.

Nikurashin, M., and S. Legg (2011), A mechanism for local dissipation of internal tides generated at rough topography, *J. Phys. Oceanogr.*, *41*(2), 378–395, doi:10.1175/2010JPO4522.1.

Oster, G. (1965), Density gradients, *Sci. Am.*, *213*, 70–76.

Polton, J., J. Smith, J. MacKinnon, and T.-M. A.E. (2008), Rapid generation of high-frequency internal waves beneath a wind and wave forced oceanic surface mixed layer, *Geophys. Res. Lett.*, *35*, L13602, doi:10.1029/2008GL033856.

Polzin, K. L., J. M. Toole, J. R. Ledwell, and R. W. Schmitt (1997), Spatial variability of turbulent mixing in the abyssal ocean, *Science*, *276*(5309), 93–96.

Prastowo, T., R. Griffiths, G. Hughes, and A. M. Hogg (2008), Mixing efficiency in controlled exchange flows, *J. Fluid Mech.*, *600*, 235–244.

Prastowo, T., R. Griffiths, G. Hughes, and A. M. Hogg (2009), Effects of topography on the cumulative mixing efficiency in exchange flows, *J. Geophys. Res.*, *114*, C08008, doi:10.1029/2008JC005152.

Price, J. F., and M. O. Baringer (1994), Outflows and deep water production by marginal seas, *Prog. Oceanogr.*, *33*(3), 161–200.

St. Laurent, L. C., H. L. Simmons, and S. R. Jayne (2002), Estimating tidally driven mixing in the deep ocean, *Geophys. Res. Lett.*, *29*(23), 2106, doi:10.1029/2002GL015633.

Sutherland, B. R., B. Lee, and J. K. Ansong (2012), Light attenuation experiments on double diffusive plumes and fountains, *Phys. Fluids*, *24*, 066605.

Trossman, D. S., S. Waterman, K. L. Polzin, B. K. Arbic, S. T. Garner, A. C. Naveira Garabato, and K. L. Sheen (2015), Internal lee wave closures: Parameter sensitivity and comparison to observations, *J. Geophys. Res. Oceans*, *120*, 7997–8019, doi:10.1002/2015JC010892.

Trossman, D. S., B. K. Arbic, J. G. Richman, S. T. Garner, S. R. Jayne, and A. J. Wallcraft (2016), Impact of topographic internal lee wave drag on an eddying global ocean model, *Ocean Modell.*, *97*, 109–128, doi:10.1016/j.ocemod.2015.10.013.

Vosper, S. B. (2004), Inversion effects on mountain lee waves, *Q. J. R. Meteorol. Soc.*, *130*(600), 1723–1748.
Waterman, S., A. C. Naveira Garabato, and K. L. Polzin (2013), Internal waves and turbulence in the Antarctic Circumpolar Current, *J. Phys. Oceanogr.*, *43*(2), 259–282, doi:10.1175/JPO-D-11-0194.1.
Winters, K. B., and L. Armi (2013), The response of a continuously stratified fluid to an oscillating flow past an obstacle, *J. Fluid Mech.*, *727*, 83–118.
Winters, K. B., and L. Armi (2014), Topographic control of stratified flows: Upstream jets, blocking and isolating layers, *J. Fluid Mech.*, *753*, 80–103.
Winters, K. B., P. N. Lombard, J. J. Riley, and E. A. Dasaro (1995), Available potential energy and mixing in density-stratified fluids, *J. Fluid Mech.*, *289*, 115–128.